Sensors and Actuators Reports 5 (2023) 100140

Contents lists available at ScienceDirect

Sensors and Actuators Reports

journal homepage: www.sciencedirect.com/journal/sensors-and-actuators-reports

Multiplexed resistive pulse sensor based on geometry modulation for high-throughput microparticle counting

Ruiting Xu [a], Leixin Ouyang [a], Rubia Shaik [b], Ge Zhang [b], Jiang Zhe [a,*]

[a] Department of Mechanical Engineering, University of Akron, Akron, OH 44325, United States
[b] Department of Biomedical Engineering, University of Akron, Akron, Ohio 44325, United States

ARTICLE INFO

Keywords:
Geometry modulation
High throughput
Particle counting
Resistive pulse sensor
Iterative cancellation
Microfluidics

ABSTRACT

While resistive pulse sensor (RPS) has been used to characterize the nano/micro-targets (cells, biomolecules, etc.) in biomedical research, one long standing drawback is its low throughput. Here we report a novel geometry modulation based RPS to improve the throughput without increasing the complexity of measurement electronics. The sensor consists of multiple parallel sensing channels whose geometries are uniquely designed based on 7-bit spreading sequences. Because of the unique geometry, when a particle passes a sensing channel, the voltage signal from this channel is encoded by a specific waveform. Only a DC source was applied, and only one combined signal from all sensing channels was collected. For demodulation, the maximum correlation coefficient between the combined signal and each template waveform was used to identify the passage of a particle from a specific sensing channel, and the occurring time of the passage. An iterative cancellation scheme was developed to extract the identified waveforms, by a series of subtractions of the identified waveforms with amplitudes from high to low, until the correlation coefficients between the remaining signal with all template waveforms became less than 0.4 (weak correlation). Mixtures of different-sized polystyrene particles were used to test the device. Results showed that the device is capable of accurately sizing and counting various microparticles with errors of 5.8% and 5.2% while the throughput was improved 300%. With the simple structure and measurement setup, the geometry-modulated RPS has great potential for the detection and analysis of a variety of micro/nano bio-objects.

1. Introduction

Resistive pulse sensors (RPSs) are widely used for fast counting and sizing of micro/nano scale targets suspended in liquids (e.g. cells [1,2], protein [1,3,4], nucleic acids [5,6], and colloidal particles [7,8]). In RPS, two electrodes in the electrolyte solution are separated by a narrow sensing channel [9]. Passage of a single particle through the sensing channel displaces a volume of the electrolyte solution and changes the impedance of the sensing channel, generating current or voltage pulses. Counts and magnitudes of the electrical pulses reflect particles' concentrations and sizes [10]. Furthermore, the shapes and durations of the pulses can be used to infer the shape of the sensing channels [11,12] and the surface charge (or zeta potential) of target particles [13]. RPS can analyse individual particles even in extremely low abundance, and thus is attractive in many bio-related research. With advances in the micro and nano fabrication of micro/nano-scaled channels, RPS has been used in detecting bio-objects such as cells [14,15], viruses [16,17], single molecules [6,7], DNA [18,19], and antibody-antigen binding [11,20]. Recently, RPSs were utilized to detect biomolecules (e.g. nucleotides and target protein [5,21,22]) in combination with aptamer functionalized nanoparticles [23,24]. Despite multiple advantages, one major limitation of RPSs with one sensing channel is their low throughput. The sensing channel must be fabricated sufficiently small for micro and nano-scaled objects to generate detectable signals. Thus only a limited amount of analyte solution can be analysed especially when targets are in nanoscale. Due to the short survival time of the bio-objects, quick analysis becomes necessary, which requires high throughput.

To improve the throughput, researchers have developed devices with multiple microchannels. Song et al. [25] proposed a differential RPS (space modulation) using eight sensing channels. This device had higher throughput due to parallel sample analysis. However, implementing individual detecting electronics for each sensing channel is impractical when more channels are needed. Jagtiani et al. [26] invented a frequency division signal multiplexing on parallel RPS for cell counting. A

* Corresponding author.
E-mail address: jzhe@uakron.edu (J. Zhe).

https://doi.org/10.1016/j.snr.2023.100140
Received 19 November 2022; Received in revised form 9 January 2023; Accepted 11 January 2023
Available online 13 January 2023

unique encoding frequency was applied to each sensing channel via a central electrode. The combined current signal was collected with a single pair of electrodes, which was subsequently demodulated by fast Fourier transform and frequency division. This method dramatically reduced the sampling data size and hardware complexity. However, the device needs to be operated within a narrow frequency range where the RPS channels are resistance dominant; only a limited number of sensing channels can be used. Liu et al. [27,28] demonstrated the microfluidic CODES (Coded Orthogonal Detection by Electrical Sensing) method for high throughput cell counting via multiple channels. When one cell passed through a channel, the resistive pulse signal was encoded by a specific spreading code waveform generated by the unique pattern of three sets of micro coplanar electrodes. The cell's occurrence and size were determined by the peak correlation coefficient between the combined signal and the code waveforms. This waveform with desired amplitude was then subtracted. This process was repeated until correlation coefficients with all code waveforms were small. One concern is that it is difficult to estimate the cell size (and the desired amplitude of signals to be subtracted) from the correlation coefficient eventually may causing errors in cell sizing and counting [29–31]. Furthermore, Wang et al. [32] demonstrated a pattern recognition method, i.e. deep convolutional neural networks, which can count particles via high density parallel channels. To train the networks, a large waveform database (e.g. over one million augmented non-interfering waveforms when various-sized particles passed through each channel at different speeds) was constructed. Deep learning-based algorithm was used to find the pattern match between the output signal and template waveforms, and thus to determine the particle sizes and occurrence time. The pattern recognition could be time-consuming because of the large size of the waveform library. Accuracy in sizing and counting particles could also be compromised due to indistinct features of the combined signal especially when multiple particles are present at the same time [33–36]. Furthermore, the above CODES methods required an AC excitation system and three sets of electrodes to generate the bipolar code signals. A lock-in amplifier was needed to extract the desired signals caused by the passage of particles, increasing the complexity of the device.

To overcome the above problems, we present a geometry modulation based resistive pulse sensor. In our strategy, each sensing channel has a unique multiple-segment geometry, which generates a unique waveform signal due to the passage of particle. The combined signal consists of signals from all individual sensing channels, which is collected, and is demodulated. The advantages of this sensor are: 1) The geometry modulation encodes signals by unique geometries without using complex electrodes and control signals, 2) While the counting throughput is improved multiple folds via its parallel sensing channels, only one DC source is needed, and only one combined signal is measured; the geometry modulation is simple and scalable, more sensing channels can be easily added to significantly improve the throughput 3) Using a unique interactive cancellation procedure, the errors in counting and sizing the particles are significantly reduced. A proof of concept, a 4-channel device was fabricated and tested to demonstrate the sensing principle. With simple structure and easy operation, the geometry-modulated RPS shows a great potential for rapid and enormous detection of micro/nano targets (e.g. blood cells or wastewater particles) in haematology and environmental applications.

2. Material and methods

2.1. Materials

10 μm (product# 72,986), 15 μm (product# 74,964), and 20 μm (product# 74,491) diameter polystyrene particles were purchased from Sigma-Aldrich. Dulbecco's phosphate-buffered saline (DPBS, 1X, product# MT21031CV, Thermo Fisher Scientific) was used to prepare the particle solution. Nonionic surfactant (CAS 9002–93–1, FisherBiotech) was used to avoid particle aggregation.

2.2. Sensing principle

To achieve multiplexed detection of different-sized microparticles, we designed a geometry modulation RPS with four sensing channels, as shown in Fig. 1a. The narrow segment has a larger resistance (or larger voltage), while the wide segment has a smaller resistance (or smaller voltage). Hence the narrow and wide segments can be used to represent bits of '1' and '0' respectively. For the design of sensing channels, each sensing channel has a unique geometry that matches one specific spreading sequence code. When a particle transits each sensing channel, the change in the channel resistance is detected, and voltage change is encoded with a unique waveform or spreading code. The ideal waveform for each sensing channel is shown in Fig. 1c (black curve). The actual waveforms representing the spreading codes are more complex, which are discussed in Fig. S1 in Supplementary Information. Fig. 1c (blue curve) shows the actual waveforms when a 10 μm particle passed through the four individual sensing channels (spreading code 1010110, 1101100, 0111111, and 1110100) separately. For the multichannel device, the combined signal, consisting of signals from all sensing channels is collected.

A DC Wheatstone bridge was used to measure the combined resistive pulse signal, as shown in Fig. 1b. R_{ch} represents the resistance of the RPS, and R_2 is the external adjustable resistance. R_3 and R_4 are fixed value resistors, and the values are set to be 1kΩ to form a Wheatstone bridge. Before each test, R_2 was adjusted to be equal to R_{ch}, so that the voltage drop between A and B (V_{AB}) was zero. A DC voltage, V_{in}, is applied to the circuit. When particles transit the sensing channels, a resistance change in R_{ch} is generated which causes a change in V_{AB}. This voltage change is amplified and measured as V_{out}.

For the multiple channels connected in parallel, the combined signal is a sum of individual signals from all sensing channels. To demodulate the combined signal, the combined signal is correlated with the template waveform of each channel with a unique spreading code. If a particle passes one specific channel, the correlation coefficient with the desired code (i.e., the unique waveform of one sensing channel) is higher than those with other codes. Hence the signal of this channel can be isolated and subtracted from the combined signal. This procedure is continued until the correlation coefficient between the remaining signal with all spreading codes is low (e.g. <0.4, weak correlation) [37], indicating the remaining signal contains no obvious waveform of any sensing channel. Note that we used a peak correlation of 0.4 as the sign to evaluate the similarity between two signals. This sign was well studied and determined by prior statistical research [37] and widely accepted by medical applications [38,39]. A larger than 0.4 correlation coefficient typically indicates a strong relation between signals, phenomena, or statistical variables [37,38].

2.3. Spreading sequences

In this paper, 1010110, 1101100, 0111111, and 1110100 were used for the design of four sensing channels and encoding the electrical signals from each sensing channel. These four codes were generated from a preferred pair of m-sequences (1001011 and 1110100), and then shifted one bit of the second m-sequence cyclically and performed XOR operation [40].

To demodulate the combined signals, first, template waveforms generated by a standard particle (e.g. 10 μm particle) passing through each individual sensing channel (without the presence of any neighbouring sensing channel) were measured at one constant flow rate. Next, these four template waveforms were used as template waveforms to correlate with the detected combined signals. If one particle is present in a channel, the correlation with this channel's sequence waveform will generate a high correlation coefficient. The correlation coefficient function between two series of data has been shown in Eq. (1) [41].

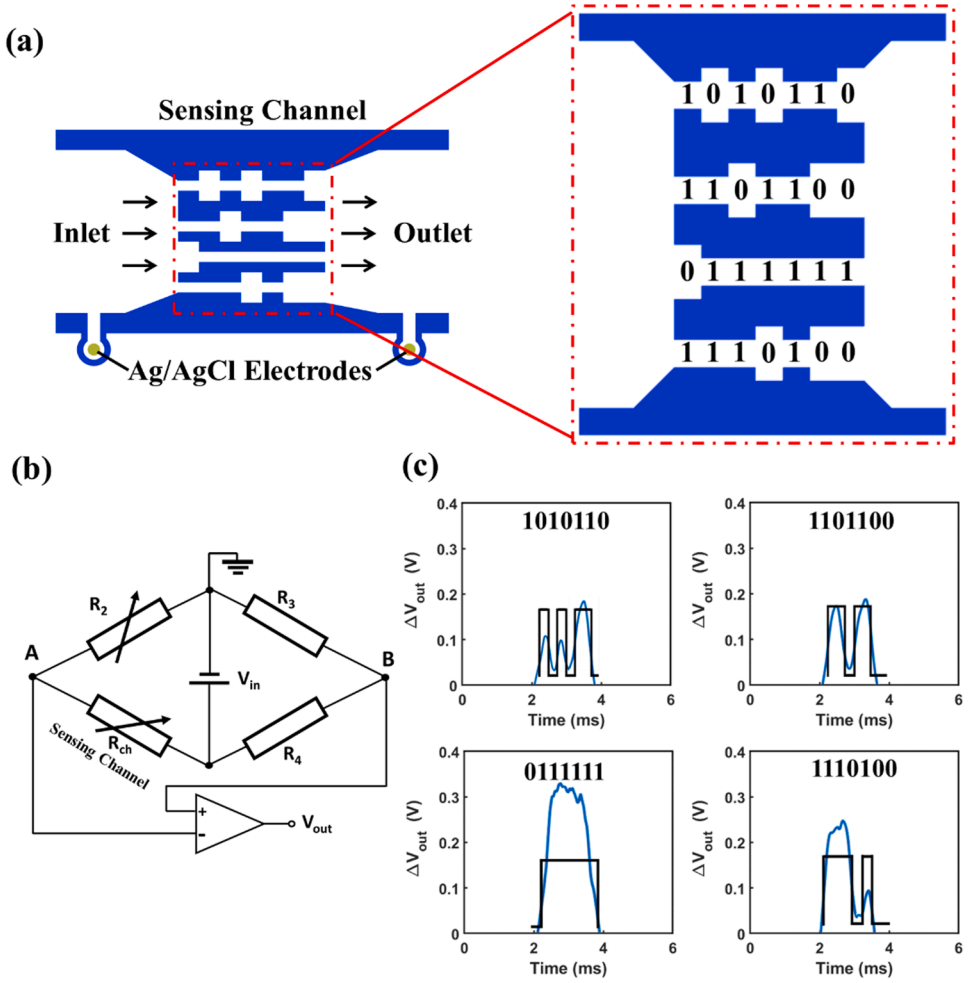

Fig. 1. Schematic of the microfluidic sensor for particle analysis. (a) Illustration of the geometry modulation sensor with four parallel sensing channels and enlarged image of sensing channel. A narrow segment represents bit '1' and a wide segment represent bit '0'. (b) Diagram of circuit to measure the resistive changes generated by particle transiting a sensing channel. The input voltage V_{in} was set to 1 V to avoid hydrolysis of DPBS. (c) Electrical waveforms when a particle transits through each sensing channel with a unique spreading sequence code. Spreading sequence codes (black) are used: 1010110, 1101100, 0111111, and 1110100. Blue: measured electrical signals coming from particles passing through each channel.

$$r_{xy} = \frac{\sum(x_i - x_m)\cdot(y_i - y_m)}{\sqrt{(x_i - x_m)^2\cdot(y_i - y_m)^2}} \quad (1)$$

Where x_i and y_i represent each set of data, i from 1 to N (last element). x_m and y_m are the averages of data value ($x_m = N^{-1}\cdot\sum x_i$ and $y_m = N^{-1}\cdot\sum y_i$). The correlation coefficient value ranges between +1.0 (perfect positive correlation) and −1.0 (perfect negative correlation).

One challenge is that particles may pass one sensing channel at different speeds because of variations in their sizes, axial positions, or driving pressure. Hence the durations of the waveform patterns of these particles are different. On the other hand, when several particles are present in separate sensing channels, the combined signal has a longer duration than the template waveforms of each individual channel. To address this problem, the four template waveforms collected when one particle passes through each individual channel are processed by a custom MATLAB program to generate these waveforms with various durations. The duration can be shrunk or elongated by multiplying the time interval between two data points by a constant factor (e.g. from 0.5 to 2 with an incremental interval of 0.1). To identify whether the combined signal contains the specific waveform, the combined signal is correlated with the generated template waveforms with different durations. Only the maximum/peak correlation coefficient is considered. A peak coefficient larger than 0.4 indicates that at this moment, a particle passes the channel, so that the combined signal has a strong similarity with the waveform of this channel [37]. From the correlation analysis, the presence of particles in individual channels can be determined.

Once the desired waveform is determined, it should be subtracted from the combined signals. However, due to the unknown sizes of particles, the amplitude of the waveform is difficult to be determined. While researchers attempted to use the peak correlation coefficient to determine the sizes [29–31], this method is likely to cause errors in particle sizes and counts because the presence of particles in the neighbouring channels significantly affects the correlation coefficient. An example is shown in Supplemental Information (Fig. S2). Here we use an interactive cancellation method. Since the template waveforms were obtained from a 10 μm particle, the amplitudes of the waveforms of each channel were defined as 1 × magnitude. In the interactive cancellation, once a waveform match is determined, only a fraction of the magnitude (e.g. 0.8 × amplitude) is subtracted from the combined signal. After the subtraction, correlation analysis is conducted again; if the correlation coefficient is still larger than 0.4, additional subtraction of this waveform with the 0.8 × amplitude is performed from the remaining signal. This process is repeated until the correlation coefficients between the remaining signal and four template waveforms are less than 0.4. However, if after the latest subtraction, the correlation coefficient becomes high negative (<−0.4), this indicates an over subtraction of the waveform. The 0.8 × subtraction needs to be replaced by a 0.4 × subtraction. If 0.4 × subtraction still causes a high negative correlation coefficient, a 0.2 × subtraction should be used. This procedure is repeated until the absolute value of the peak correlation coefficient less than 0.4 is achieved. In this paper, 0.4 is used as a threshold to judge the similarity between the combined signal and the template waveforms. When the absolute value of the correlation coefficient is less than 0.4, the similarity between the two signals is considered weak [37]. The size of the particle is then determined from the overall amplitude of this waveform

subtracted from the combined signal. In the results and discussion section, we will use several cases where different-sized particles are present in different sensing channels to further illustrate the interactive cancellation process.

The advantage of using the interactive cancellation is that it does not rely on the correlation coefficient to determine the particle size, which is likely to cause errors because the correlation coefficient is not only affected by the size of the particle present in the desired channel, but also affected by the presence of particles in neighbouring channels. Using the interactive method, the size of the particle can be accurately determined.

2.4. Device fabrication

The standard soft lithography method was used to fabricate the geometry modulation sensor, as shown in Fig. 2. An SU-8 2025 (Micro-Chem, MA, USA) mould was fabricated, consisting of (1) four sensing channels with different geometries, (2) two Ag/AgCl electrode holes to place the electrodes to measure the resistance change caused by particles passing through the sensing channel, and (3) inlet/outlet reservoirs and connection channels. The seven segments of each sensing channel were designed based on the chosen spreading sequence codes. Each segment represents one bit. The length of each segment/bit is set to be 20 μm. Thus, the total length of one seven-bit sensing channel is 140 μm. The widths of the segment '1' and '0' (or bit) are 40 μm and 100 μm respectively. The height of the device is 30 μm everywhere. The microfluidic RPS was fabricated via pouring polydimethylsiloxane (PDMS, Dow Corning Sylgard 184 Silicone Elastomer Kit) onto the SU-8 mould followed by degassing and curing the PDMS for 2 h at 70 °C in a vacuum chamber. Then the inlet/outlet reservoirs and electrode holes were created by punching the PDMS slab with biopsy punches in 1.5 mm and 1 mm diameter respectively. Subsequently the PDMS slab was bonded onto a glass substrate after treatment with air plasma (200 mTorr, 50 W, 50 s). The dimensions of the sensing channel measured by the profilometer (Dektak 150, Veeco Instrument, NY, USA) are 33.17 ± 1.35 μm (height), 138.15 ± 2.27 μm (length). The widths of segments '1' and '0' are 41.59 ± 1.18 μm and 102.16 ± 1.87 μm. Finally, two Ag/AgCl electrodes (1mm diameter) were placed into the electrode holes to measure the resistive pulses and complete the geometry modulation sensor. For each test, the particle solution was loaded into the inlet reservoir and driven through the sensor by a constant pressure of 2 kPa. A DC voltage (1 V) was applied across the Ag/AgCl electrodes to avoid hydrolysis of DPBS, resulting in the fluctuation of flow. The voltage pulse signals by the particles were amplified with a differential amplifier (AD620BN, analog Devices Inc, USA), recorded with an NI – DAQ board (PCI-6133, National Instrument USA) at a sampling rate of 500 kHz via data acquisition software (LabVIEW, National Instruments). The recorded signals were processed using a custom MATLAB program to denoise and analyse.

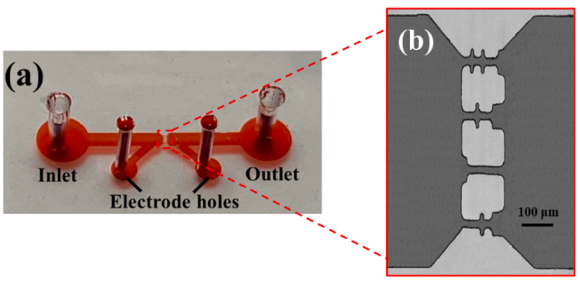

Fig. 2. Images of the geometry modulation RPS. (a) Picture of the complete microfluidic device with four parallel detections. (b) Microscopic image of four sensing channels.

3. Results and discussion

3.1. Validation of geometry modulation method

To demonstrate the principle of geometry modulation, the mixed solutions of three different-sized polystyrene particles including 10 μm (10 ± 0.2 μm), 15 μm (15 ± 0.2 μm), and 20 μm (20 ± 0.3 μm) were used, and loaded into the device. To validate the geometry modulation method, a high-speed camera (MU043M-FL, United Scope LLC) was used to capture the transits of particles through the sensing channels. These images were used to validate the presence and sizes of the particles. Before the demodulation, waveforms, when a 10 μm microparticle passed through each individual sensing channel, were collected as the template waveforms. These waveforms are shown in Fig. 1c (blue).

Fig. 3 shows the decoding procedures for a case where only one particle was present in a channel (Fig. 3 a1). The combined voltage signal is shown in Fig. 3 b1. To determine the sensing channel where the particle passed, correlations between the detected signal and the four template waveforms were conducted (Fig. 3 a2). The maximum correlation coefficient, occurred in channel 3, indicating the particle presence occurred in channel 3. Next, a 0.8 × waveform of channel 3 was subtracted from the detected signal. Fig. 3 b2 shows the remaining signal after the first subtraction. The correlation analysis was conducted again with all template waveforms, and the maximum correlation coefficient still occurred in channel 3 (Fig. 3 a3). A second 0.8 × subtraction of waveform 3 was processed (Fig. 3 b3), and the correlation coefficient between the remaining signal and four template waveforms became a large negative value (−1, absolute magnitude is larger than 0.4), as shown in Fig. 3 a4, implying an over subtraction occurred. Thus, a 0.4 × waveform 3 was subtracted to replace the 0.8 × subtraction (Fig. 3 b4), and a negative correlation coefficient (−1) still occurred (Fig. 3 a5). Next, we tried a 0.2 × waveform 3 subtraction (Fig. 3 b5), the remaining signal still generated a negative correlation coefficient less than −0.4 (Fig. 3 a6). Hence a 0.1 × subtraction of waveform 3 was conducted (Fig. 3 b6); After the subtraction, the correlation coefficient with waveform 3 became positive but was still higher than 0.4 (Fig. 3 a7). Subsequently, a 0.05 × waveform 3 was subtracted (Fig. 3 b7). We did not subtract an additional 0.1 × waveform 3 because in the previous steps (Fig. 3 b5), subtracting a 0.2 × waveform 3 would cause an over subtraction (See Fig. 3 a6). After that the 0.05 × subtraction (Fig. 3. b7), all correlation coefficients became less than 0.4 but all positive (Fig. 3 a8); the iterative cancellation procedures were completed. Overall a 0.95 × waveform 3 was subtracted after no similarity was found between the combined signal and all four template waveforms. While the magnitude of the waveform is proportional to the particle volume, the corresponding size of the particle was calculated to be 9.8 μm. Note that here we utilized 0.4 as a threshold value to determine where there is a similarity between the remaining signal and the template waveforms [37].

Fig. 4 a1 shows two different-sized particles passing through two sensing channels simultaneously. Fig. 4 b1 shows the combined signal from all channels. To demodulate the signal, first, the correlation between the combined signal and each template waveform was conducted. Fig. 4 a2 shows the correlation coefficients with all four template waveforms, showing the maximum correlation occurred in channel 4. Next, a subtraction of 0.8 × waveform of channel 4 was operated from the combined signal. Fig. 4 b2 shows the remaining signal. A correlation analysis was conducted again with all channels' waveforms (see Fig. 4 a3), showing that the maximum correlation still occurred in channel 4. One more 0.8 × subtraction from the remaining signal was done, as shown in Fig. 4 b3. After three subtractions of 0.8 × of template waveform 4 (Fig. 4 b4), the maximum correlation coefficient occurred in channel 1 (see Fig. 4 a5). Hence a subtraction of 0.8 × of template waveform 1 was processed (Fig. 4 b5). After the subtraction, the maximum correlation occurred in channel 4 again (Fig. 4 a6). A subtraction of 0.8 × waveform 4 was conducted (Fig. 4 b6), resulting in the

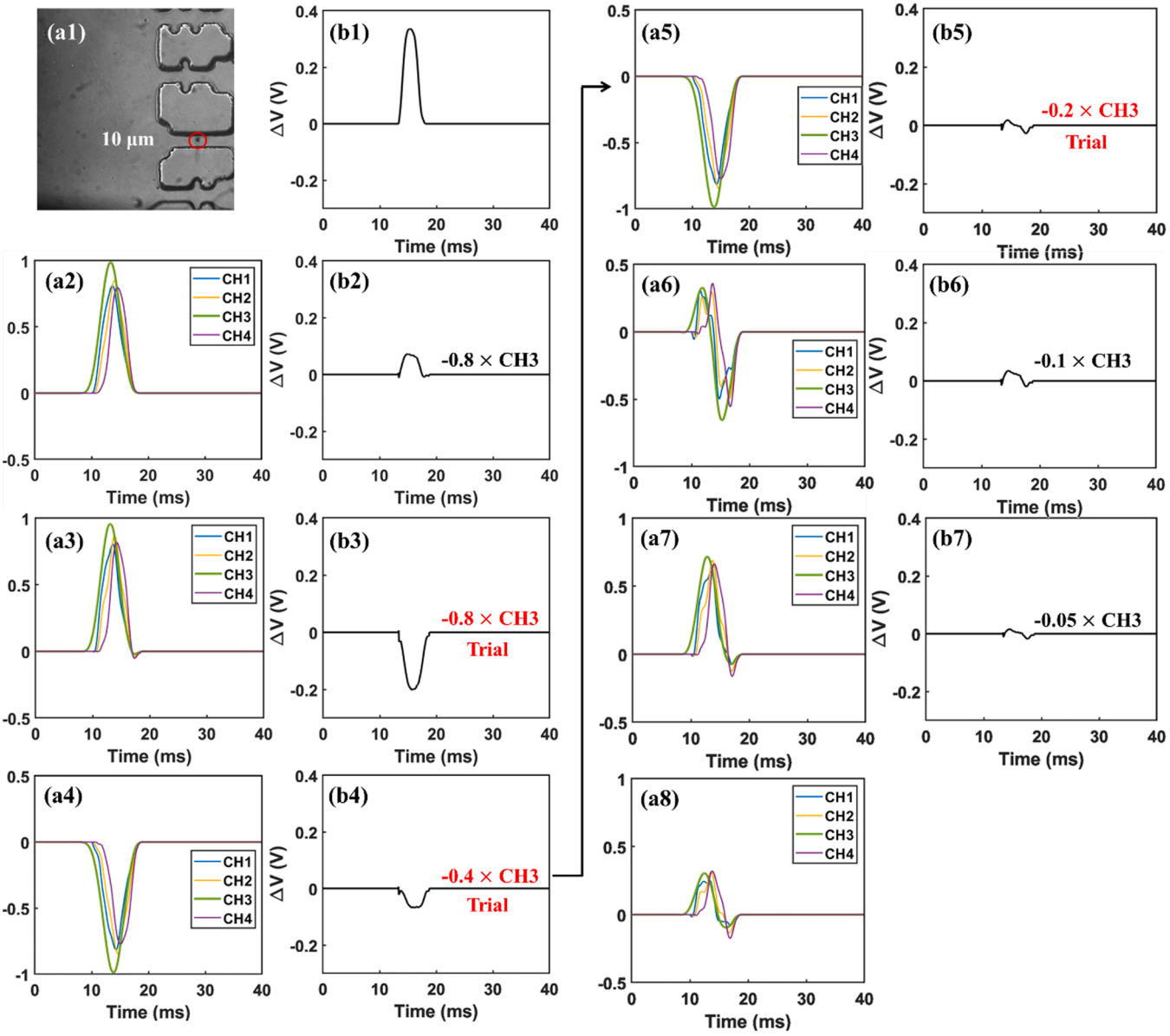

Fig. 3. Iterative cancellation procedures for decoding the combined electrical signal generated by one single particle. During the cancellation, the combined signal was correlated with four template waveforms with different durations. Based on the correlation coefficient, the desired waveform of the sensing channel where the particle was present was determined. Next, the desired waveform with 0.8 × base amplitude was subtracted from the combined signal. This correlation-subtraction process was operated until all correlation coefficients between the remaining signal and four template waveforms became less than 0.4. Waveforms with smaller amplitude (e.g. 0.4 × , 0.2 × ,0.1 × , 0.05 ×) were subtracted in case a negative correlation coefficient (which indicates an over subtraction) was generated. Subtractions marked by red represented trial subtractions, which would cause an over subtraction, and were not conducted. Subtractions marked by black represented actual subtractions from the combined signal.

maximum correlation coefficient occurring in channel 1 (Fig. 4 a7). As shown in Fig. 4 b7, when the 2nd subtraction of 0.8 × of waveform 1 was attempted, the correlation coefficient became −0.8 (Fig. 4 a8), indicating this is an over subtraction. Then, a 0.4 × subtraction of waveform 1 was used to replace 0.8 × subtraction (Fig. 4 b8). After that, the maximum correlation coefficient occurred in channel 4 (Fig. 4 a9). When subtracting 0.8 × waveform 4 was attempted (Fig. 4 b9), a large negative correlation coefficient occurred again (−0.85), as shown in Fig. 4 a10. Thus a 0.4 × subtraction of waveform 4 was tried to replace 0.8 × subtraction (Fig. 4 b10), which still generated a large negative correlation coefficient, i.e. −0.7 (Fig. 4 a11). We further replaced the 0.4 × subtraction with a 0.2 × subtraction (see the remaining signal in Fig. 4 b11). After the subtraction, the absolute correlation coefficients with all template waveforms were less than 0.4 (Fig. 4 a12), indicating there is no similarity between the remaining signal and all four template waveforms. Note that the magnitude of the resistive pulse magnitude is proportional to the volume of the particle. From the overall subtracted magnitudes of channel 1 (1.2 ×) and channel 4 (3.4 ×), the particle sizes were estimated to be 10.6 μm and 15.04 μm in channel 1 and channel 4 respectively, which are in good agreement with the actual particle sizes (10 and 15 μm). The maximum error of particle size is 6%.

Note that we also used the same interactive cancellation procedures to demodulate the combined signals for cases where three particles and four particles were present simultaneously in separate 3 and 4 sensing channels respectively. The optical image of the particles' presence, the combined signal, and the demodulate results are shown in Fig. 5a and 5b. The detailed demodulation procedures are shown in Supplementary Information (S3 and S4) due to the lengthy steps. For three particle case,

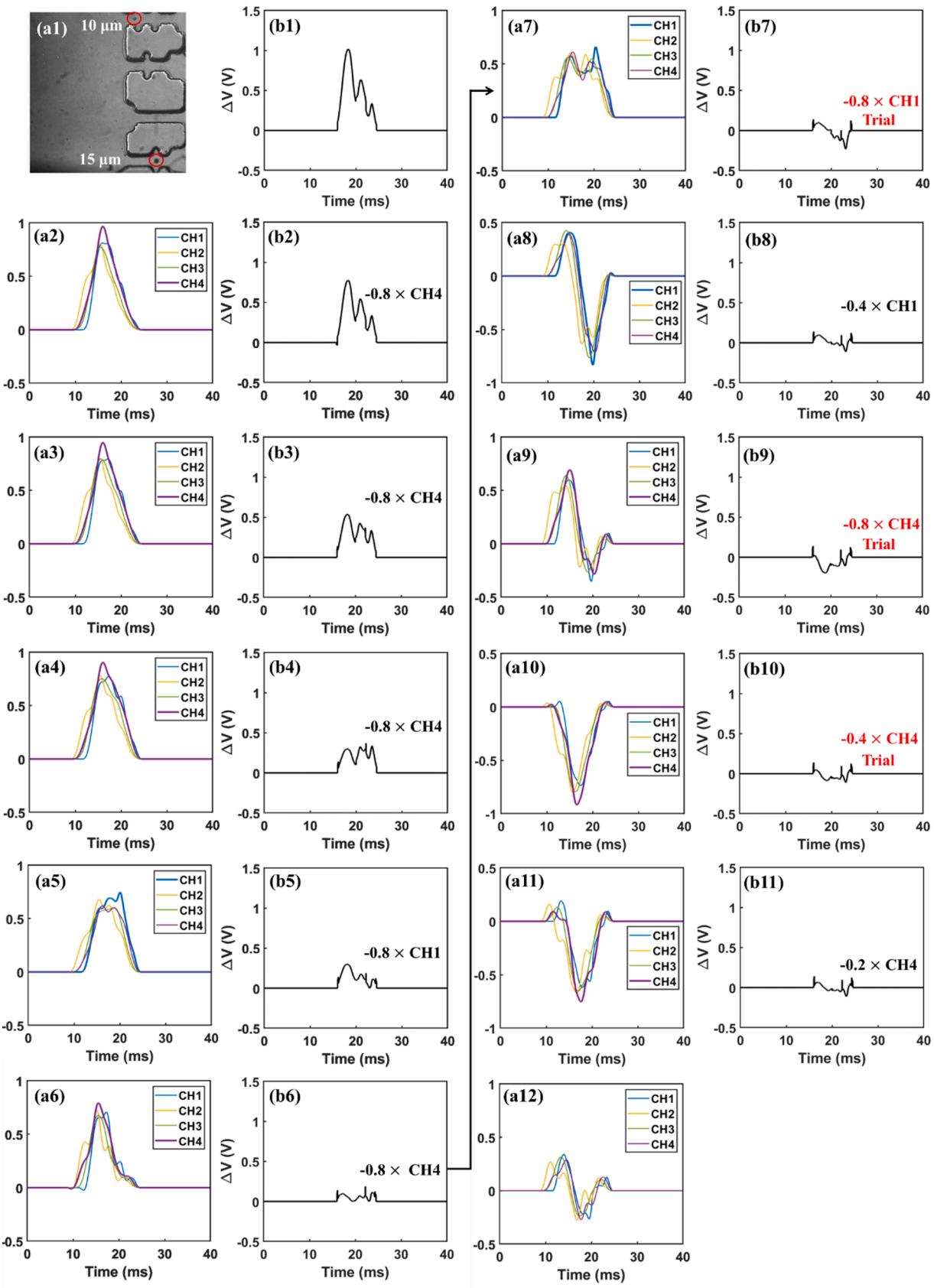

Fig. 4. Iterative cancellation procedures for decoding the combined signal generated by two particles of different sizes. Subtractions marked by red represented trial subtractions, which would cause an over subtraction, and were not conducted. Subtractions marked by black represented actual subtraction from the combined signal.

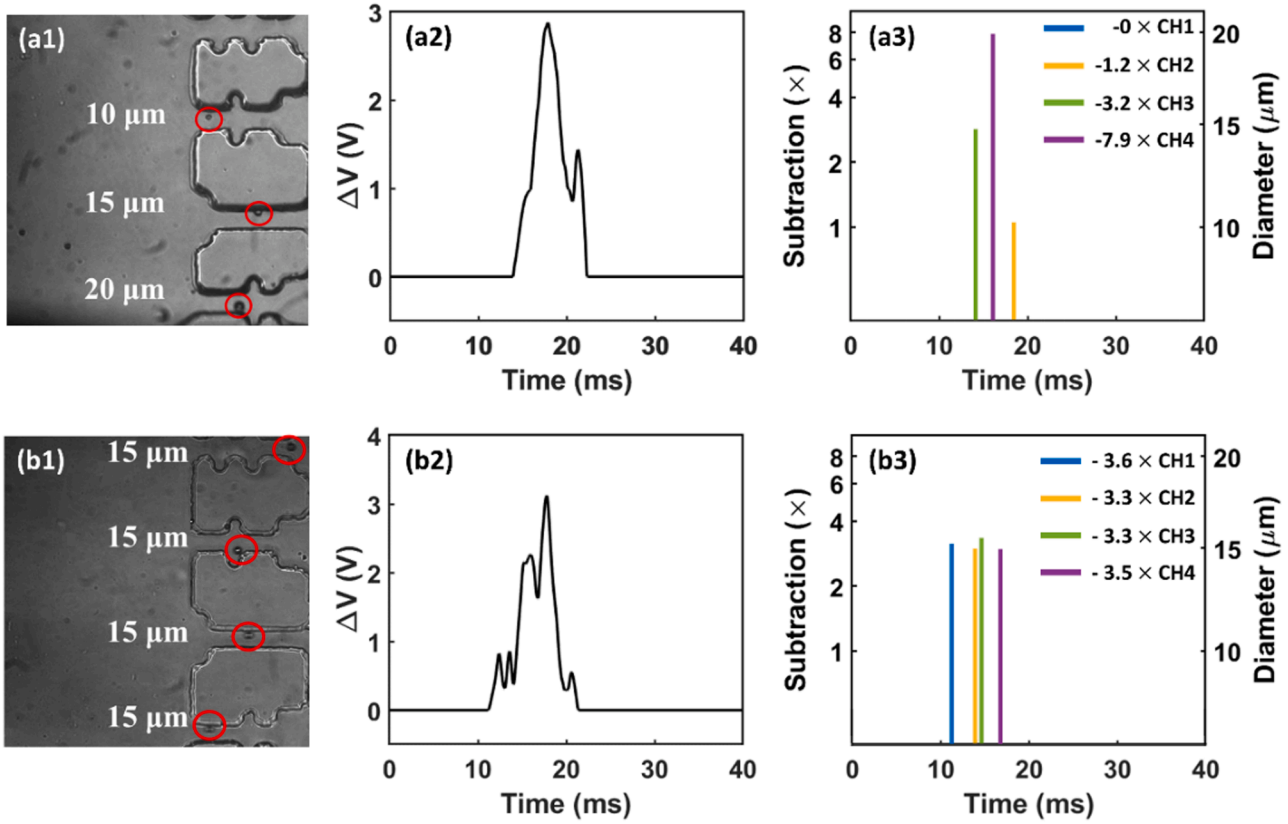

Fig. 5. Results in decoding electrical signals generated by multiple particles of different sizes. Left: optical image for different-sized particles. Middle: detected combined electrical signal. Right: iterative cancellation results and the corresponding diameters. (a) three coincident particles. (b) four coincident particles.

the calculated particle sizes were 10.3 μm (channel 2), 14.73 μm (channel 3), and 19.9 μm (channel 4). For four particle case, the measured particle diameters are 15.03 μm (channel 1), 14.73 μm (channel 2), 15.3 μm (channel), and 14.73 μm (channel 4). The measured particle sizes are in good agreement with the actual particle sizes with a maximum error of 3%.

Note that we chose an initial 0.8 × subtraction for the interaction cancellation to reduce the number of the interactions and to achieve the decent resolution for particle sizing. Other initial subtractions (e.g. 0.5 × , 0.3 ×) can also be used. We tried both 0.5 × and 0.3 × initial subtractions and obtained very similar particle counts and sizes. Also, since all waveforms used are not standard binary digital waveforms, the correlation coefficients between each of them were larger than 0.4. Only the maximum correlation coefficient was applied to judge the similarity with the desired waveform. The subtracted waveform for each round of cancellation was the one that generated the highest correlation coefficient with the remaining combined signal.

3.2. Demonstration of size and counting accuracy

Three different mixed particle solutions were used to demonstrate the sizing and counting accuracy of the four-channel RPS. Each mixed solution was prepared by mixing the three-sized particles (10 ± 0.2 μm, 15 ± 0.2 μm, 20 ± 0.3 μm) with different concentrations. Each particle mixture was loaded to the device; the combined signal was collected continuously, which was demodulated subsequently as described in Fig. 3 and 4. Particle counts and sizes were obtained. The particle concentration was determined by dividing the particle counts by the flow rate. The measured particle concentrations and sizes are shown in Fig. 6. The error bar represents the standard deviation of three separate measurements of each solution with known particle concentrations. The measured concentrations were 58.1 ± 3.37 MP/μL (20 μm particles),

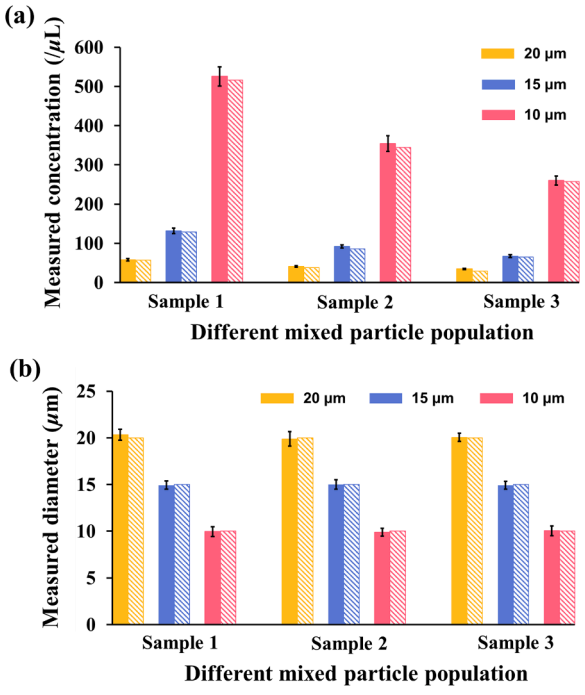

Fig. 6. Comparison of measured and actual concentrations and diameters of micro particles in the mixed solution. (a) comparison of measured particle concentration vs actual particle concentration, (b) comparison of measured particle diameter vs actual particle diameter. Actual particle concentrations and sizes (represented by rectangular boxes with slash lines) were measured by AccuSizer™ 780 (Optical Particle Sizer).

132.2 ± 6.88 MP/μL (15 μm) and 525.7 ± 24.3 MP/μL (10 μm) for Sample 1; 40.9 ± 2.31 MP/μL (20 μm), 91.9 ± 3.88 MP/μL (15 μm) and 354 ± 19.83 MP/μL (10 μm) for Sample 2; 34.7 ± 1.59 MP/μL (20 μm), 67.3 ± 3.5 MP/μL (15 μm) and 260.3 ± 11.36 MP/μL (10 μm) for Sample 3. In comparison, the actual particle concentrations of all samples were measured by AccuSizer™ 780 (Optical Particle Sizer). The actual concentrations were represented in Fig 6a as rectangular bars with slash lines. Apparently, the actual concentrations and the measured concentrations are in good agreement. The standard deviation of errors in particle counting is 5.8%. This is possible because polystyrene microparticles used in the tests have a density (1.05×10^3 kg/m^3) slightly higher than water, a small amount of particles may be deposited on the substrate due to gravity before passing the sensing channels.

The particle size measurement result is shown in Fig. 6b. The measured microparticle sizes were 20.33 ± 0.57 μm, 14.94 ± 0.44 μm and 9.96 ± 0.52 μm for Sample 1; 19.89 ± 0.77 μm, 15.01 ± 0.49 μm and 9.9 ± 0.42 μm for Sample 2; 20.05 ± 0.43 μm, 14.92 ± 0.41 μm and 10.05 ± 0.51 μm for Sample 3. The actual concentrations measured by AccuSizer™ 780 (Optical Particle Sizer) were 57 MP/μL (20 μm), 129 MP/μL (15 μm) and 516 MP/μL (10 μm) for Sample 1; 38 MP/μL (20 μm), 86 MP/μL (15 μm) and 344 MP/μL (10 μm) for Sample 2; 29 MP/μL (20 μm), 65 MP/μL (15 μm) and 258 MP/μL (10 μm) for Sample 3, which are plotted as rectangular bars with slash lines. Both measured particle sizes are in good agreement with the actual sizes, with a maximum error of 5.2%. The results further confirmed the accuracy of the device and demonstrated the feasibility of the geometry modulation principle. The standard deviation of errors in sizing is 5.2%. The errors of particle sizing may be attributed to the following three major reasons: 1) Magnitudes of resistive pulses could be affected by the off-axis position of microparticle [7,42]. Not all particles passed the sensing channel via the centerline. 2) The microparticles used in the experiments have standard deviation in sizes (i.e. 10 ± 0.2 μm, 15 ± 0.2 μm, 20 ± 0.3 μm), and 3) The flow fluctuation could induce noises to the measured signals [7,43,44], which may cause additional errors in sizing.

The above tests demonstrated the utility of the geometry modulation based RPS in measuring the sizes ad counts of microparticles in a mixed solution. The sizes of the particles were determined by a new interactive correlation-cancellation process. The iterative cancellation method is based on an assumption that at one time only one particle is present in one sensing channel. The standard template is obtained when one particle passes through each sensing channel. If multiple particles are present in one sensing channel at one time, the resistive pulse signal would not match well with the template waveforms. This may cause errors in determining the similarity between the actual signal and the template waveforms. It is worth mentioning that in geometry modulation, since each bit of the sequence code is enabled by only one channel segment, the channel length can be designed relatively short compared to CODES [27]. Hence the chance that simultaneous passage of multiple particles in a long channel is reduced; so is misjudgement of multiple small particles as one large particle. One can also dilute particle solution to a lower concentration to further mitigate this problem. In addition, the iterative cancellation scheme can achieve the same accuracy in counting and sizing even if the sizes of the detected particles are unknown. In fact, during decoding the combined signal, the magnitude of the signal from each individual channel was unknown, which was determined by the total subtractions from the iterative cancellation scheme. The particle size was subsequently calculated from the signal magnitude. While the template waveforms from the sensing channels (with unique geometries) are non-standard binary digital signals, the experiment results still show decent match between the measured and actual sizes and concentrations of particles.

The 4-channel device presented here improved the counting throughput by 300% compared to a single channel device. The geometry modulation is simple and scalable; the throughput can be further improved by adding more sensing channels with unique geometries. Compared to other RPS modulation methods (space modulation [25], frequency division [26], CODES [27], pattern recognition [32]), this method has many advantages. Compared to space modulation method [25], a large number of sensing channels can be added for higher throughput without increasing the complexity of detection electronics. Compared to frequency modulation [26], our method does not need multiple external AC demodulation signals applied to each sensing channel, and a resistance-dominant frequency range for accurate particle sizing; only one DC source was needed; the detection electronics were significantly simplified. Compared to CODES multiplexing (Liu et al. [27,28]), unique signal patterns were obtained using only one DC source with our method; only one pair of sensing electrodes was needed to encode and decode signals. In addition, as this method does not rely on the peak correlation coefficient to estimate the particle size, the particle counting and sizing accuracy were dramatically improved without worrying the influence of the neighbouring particles on correlation coefficient. Further, in comparison to the pattern recognition method developed by Wang et al. [32], this method does not need to train the networks with a large waveform database (e.g. over one million augmented non-interfering waveforms). Since our method only required a small number of waveforms, the signal processing time was much reduced. Errors in sizing and counting particles were also reduced because no complex pattern recognition was needed.

Note that the sensor based on geometry modulation could achieve high-throughput counting for micro/nano targets. Compared to other methods (e.g. CODES [27], pattern recognition method [32]), the template library was small, which reduced the amount of correlations with the template waveforms. We conducted a test on the time required to decode one combined resistive pulse; the decoding took approximately 0.3 ms to 0.5 ms using a desktop (Intel® Core™ i5–10,400 CPU @ 2.90 GHz, 16GB Memory). The processing speed was sufficiently fast to analyse the micro/nanoparticles in real time, considering the pulse width of one combined pulse was approximately 1 ms to 2 ms. The simple structure and measurement setup make it suitable for rapid and enormous analysis of micro/nano-targets in several applications, including but not limited to blood cell detection in haematology [45,46], microsphere and cancer cell detections in pharmacology [47,48], wastewater particle analysis, pollen and algae detection in environmental monitoring [49–53].

4. Conclusions

We presented a geometry modulation-based resistive pulse sensor that enabled high throughput counting and sizing of microparticles with its four parallel sensing channels. The geometry of each sensing channel was uniquely designed based on four different spreading codes. When particles passed through the sensing channel, the electrical signals from each sensing channel were encoded by specific waveform patterns. Only one DC source is needed. The combined signal consisting of four encoded signals from the parallel sensing channels was measured. The combined signal was then demodulated by correlating the combined signal with the template waveforms from each individual channel. The maximum correlation coefficient was utilized to identify the components of the specific waveforms and durations. A new iterative cancellation scheme was developed to subtract the specific waveforms with a series of magnitudes (from high to low) until all correlation coefficients between the remaining signal with all template waveforms were small (e.g. absolute value < 0.4). This scheme does not determine the particle's size based on the absolute value of the correlation coefficient, which typically causes errors in sizing and counting the particles. We validated the device with the mixed solutions of 10 μm, 15 μm, and 20 μm polystyrene particles with known concentrations. With the standard deviation errors of 5.8% and 5.2% in concentration and size measurements, the results demonstrated the ability of the sensor in accurately measuring particles' sizes and concentrations in a mixed solution. The geometry modulation sensor without complex components, showed great potential in the detection and analysis of micro/nano-targets with

high throughput and sensitivity.

Declaration of Competing Interest

The authors declare that they have no known competing financial interests or personal relationships that could have appeared to influence the work reported in this paper.

The authors declare the following financial interests/personal relationships which may be considered as potential competing interests:

Jiang Zhe reports financial support was provided by National Science Foundation.

Data availability

Data will be made available on request.

Acknowledgements

This work was supported by the National Science Foundation of USA under award numbers DBI 1911526 and ECCS 1905786.

Appendix A. Supplementary information

Supplementary information to this article can be found.

Supplementary materials

Supplementary material associated with this article can be found, in the online version, at doi:10.1016/j.snr.2023.100140.

References

[1] H. Bayley, C.R. Martin, Resistive-pulse sensing-from microbes to molecules, Chem. Rev. 100 (7) (2000) 2575–2594, https://doi.org/10.1021/cr980099g.
[2] R. Pan, K. Hu, R. Jia, S.A. Rotenberg, D. Jiang, M.V. Mirkin, Resistive-pulse sensing inside single living cells, J. Am. Chem. Soc. 142 (12) (2020) 5778–5784, https://doi.org/10.1021/jacs.9b13796.
[3] L.T. Sexton, L.P. Horne, S.A. Sherrill, G.W. Bishop, L.A. Baker, C.R. Martin, Resistive-pulse studies of proteins and protein/antibody complexes using a conical nanotube sensor, J. Am. Chem. Soc. 129 (43) (2007) 13144–13152, https://doi.org/10.1021/ja0739943.
[4] L.T. Sexton, H. Mukaibo, P. Katira, H. Hess, S.A. Sherrill, L.P. Horne, C.R. Martin, An adsorption-based model for pulse duration in resistive-pulse protein sensing, J. Am. Chem. Soc. 132 (19) (2010) 6755–6763, https://doi.org/10.1021/ja100693x.
[5] E.L. Blundell, R. Vogel, M. Platt, Particle-by-particle charge analysis of DNA-modified nanoparticles using tunable resistive pulse sensing, Langmuir 32 (4) (2016) 1082–1090, https://doi.org/10.1021/acs.langmuir.5b03024.
[6] C.C. Harrell, Y. Choi, L.P. Horne, L.A. Baker, Z.S. Siwy, C.R. Martin, Resistive-pulse DNA detection with a conical nanopore sensor, Langmuir 22 (25) (2006) 10837–10843, https://doi.org/10.1021/la061234k.
[7] D. Kozak, W. Anderson, R. Vogel, M. Trau, Advances in resistive pulse sensors: devices bridging the void between molecular and microscopic detection, Nano Today 6 (5) (2011) 531–545, https://doi.org/10.1016/j.nantod.2011.08.012.
[8] E. Weatherall, G.R. Willmott, Applications of tunable resistive pulse sensing, Analyst 140 (10) (2015) 3318–3334, https://doi.org/10.1039/c4an02270j.
[9] Y. Song, J. Zhang, D. Li, Microfluidic and nanofluidic resistive pulse sensing: a review, Micromachines (Basel) 8 (7) (2017), https://doi.org/10.3390/mi8070204.
[10] L. Yang, T. Yamamoto, Quantification of virus particles using nanopore-based resistive-pulse sensing techniques, Front. Microbiol. 7 (2016) 1500, https://doi.org/10.3389/fmicb.2016.01500.
[11] T. Vaclavek, J. Prikryl, F. Foret, Resistive pulse sensing as particle counting and sizing method in microfluidic systems: designs and applications review, J. Sep. Sci. 42 (1) (2019) 445–457, https://doi.org/10.1002/jssc.201800978.
[12] K.R. Balakrishnan, G. Anwar, M.R. Chapman, T. Nguyen, A. Kesavaraju, L.L. Sohn, Node-pore sensing: a robust, high-dynamic range method for detecting biological species, Lab Chip 13 (7) (2013) 1302–1307, https://doi.org/10.1039/c3lc41286e.
[13] L. Ni, R. Shaik, R. Xu, G. Zhang, J. Zhe, A microfluidic sensor for continuous, in situ surface charge measurement of single cells, ACS Sens. 5 (2) (2020) 527–534, https://doi.org/10.1021/acssensors.9b02411.
[14] E.L.C.J. Blundell, L.J. Mayne, E.R. Billinge, M. Platt, Emergence of tunable resistive pulse sensing as a biosensor, Anal. Methods 7 (17) (2015) 7055–7066, https://doi.org/10.1039/c4ay03023k.
[15] T. Zhou, Y. Song, Y. Yuan, D. Li, A novel microfluidic resistive pulse sensor with multiple voltage input channels and a side sensing gate for particle and cell detection, Anal. Chim. Acta 1052 (2019) 113–123, https://doi.org/10.1016/j.aca.2018.11.049.
[16] J. Zhou, P. Kondylis, D.G. Haywood, Z.D. Harms, L.S. Lee, A. Zlotnick, S. C. Jacobson, Characterization of virus capsids and their assembly intermediates by multicycle resistive-pulse sensing with four pores in series, Anal. Chem. 90 (12) (2018) 7267–7274, https://doi.org/10.1021/acs.analchem.8b00452.
[17] K. Zhou, L. Li, Z. Tan, A. Zlotnick, S.C. Jacobson, Characterization of hepatitis B virus capsids by resistive-pulse sensing, J. Am. Chem. Soc. 133 (6) (2011) 1618–1621, https://doi.org/10.1021/ja108228x.
[18] D. Kaya, A. Dinler, N. San, K. Kececi, Effect of pore geometry on resistive-pulse sensing of DNA using track-etched PET nanopore membrane, Electrochim. Acta 202 (2016) 157–165, https://doi.org/10.1016/j.electacta.2016.04.014.
[19] M.J. Healey, W. Rowe, S. Siati, M. Sivakumaran, M. Platt, Rapid assessment of site specific DNA methylation through resistive pulse sensing, ACS Sens. 3 (3) (2018) 655–660, https://doi.org/10.1021/acssensors.7b00935.
[20] O.A. Saleh, L.L. Sohn, Direct detection of antibody-antigen binding using an on-chip artificial pore, Proc. Natl. Acad. Sci. U S A 100 (3) (2003) 820–824, https://doi.org/10.1073/pnas.0337563100.
[21] E.R. Billinge, M. Platt, Multiplexed, label-free detection of biomarkers using aptamers and tunable resistive pulse sensing (AptaTRPS), Biosens. Bioelectron. 68 (2015) 741–748, https://doi.org/10.1016/j.bios.2015.02.011.
[22] R. Xu, L. Abune, B. Davis, L. Ouyang, G. Zhang, Y. Wang, J. Zhe, Ultrasensitive detection of small biomolecules using aptamer-based molecular recognition and nanoparticle counting, Biosens. Bioelectron. 203 (2022), 114023, https://doi.org/10.1016/j.bios.2022.114023.
[23] Z. Xiao, O.C. Farokhzad, Aptamer-functionalized nanoparticles for medical applications: challenges and opportunities, ACS Nano 6 (5) (2012) 3670–3676, https://doi.org/10.1021/nn301869z.
[24] I. Heaton, M. Platt, Peptide nanocarriers for detection of heavy metal ions using resistive pulse sensing, Anal. Chem. 91 (17) (2019) 11291–11296, https://doi.org/10.1021/acs.analchem.9b02353.
[25] Y. Song, J. Yang, X. Pan, D. Li, High-throughput and sensitive particle counting by a novel microfluidic differential resistive pulse sensor with multidetecting channels and a common reference channel, Electrophoresis 36 (4) (2015) 495–501, https://doi.org/10.1002/elps.201400427.
[26] A.V. Jagtiani, J. Carletta, J. Zhe, A microfluidic multichannel resistive pulse sensor using frequency division multiplexing for high throughput counting of micro particles, J. Micromech. Microeng. 21 (6) (2011), https://doi.org/10.1088/0960-1317/21/6/065004.
[27] R. Liu, N. Wang, F. Kamili, A.F. Sarioglu, Microfluidic CODES: a scalable multiplexed electronic sensor for orthogonal detection of particles in microfluidic channels, Lab Chip 16 (8) (2016) 1350–1357, https://doi.org/10.1039/c6lc00209a.
[28] R. Liu, W. Waheed, N. Wang, O. Civelekoglu, M. Boya, C.H. Chu, A.F. Sarioglu, Design and modeling of electrode networks for code-division multiplexed resistive pulse sensing in microfluidic devices, Lab. Chip 17 (15) (2017) 2650–2666, https://doi.org/10.1039/c7lc00545h.
[29] M. Kobayashi, J. Boutros, G. Caire, Successive interference cancellation with SISO decoding and EM channel estimation, IEEE J. Selected Areas in Commun. 19 (8) (2001) 1450–1460, https://doi.org/10.1109/49.942508.
[30] P. Patel, J. Holtzman, Analysis of a simple successive interference cancellation scheme in a DS/CDMA system, IEEE J. Selected Areas in Commun. 12 (5) (1994) 796–807, https://doi.org/10.1109/49.298053.
[31] J.G. Andrews, T.H. Meng, Optimum power control for successive interference cancellation with imperfect channel estimation, IEEE Trans. Wireless Commun. 2 (2) (2003) 375–383, https://doi.org/10.1109/twc.2003.809123.
[32] N. Wang, R. Liu, N. Asmare, C.H. Chu, A.F. Sarioglu, Processing code-multiplexed Coulter signals via deep convolutional neural networks, Lab. Chip. 19 (19) (2019) 3292–3304, https://doi.org/10.1039/c9lc00597h.
[33] H.C. Shin, H.R. Roth, M. Gao, L. Lu, Z. Xu, I. Nogues, J. Yao, D. Mollura, R. M. Summers, Deep convolutional neural networks for computer-aided detection: CNN architectures, dataset characteristics and transfer learning, IEEE Trans. Med. Imaging 35 (5) (2016) 1285–1298, https://doi.org/10.1109/TMI.2016.2528162.
[34] H. Song, Q. Liu, G. Wang, R. Hang, B. Huang, Spatiotemporal satellite image fusion using deep convolutional neural networks, IEEE J. Selected Topics in Appl. Earth Observ. Remote Sens. 11 (3) (2018) 821–829, https://doi.org/10.1109/jstars.2018.2797894.
[35] M. Anthimopoulos, S. Christodoulidis, L. Ebner, A. Christe, S. Mougiakakou, Lung pattern classification for interstitial lung diseases using a deep convolutional neural network, IEEE Trans. Med. Imaging 35 (5) (2016) 1207–1216, https://doi.org/10.1109/TMI.2016.2535865.
[36] H. Sharma, N. Zerbe, I. Klempert, O. Hellwich, P. Hufnagl, Deep convolutional neural networks for automatic classification of gastric carcinoma using whole slide images in digital histopathology, Comput. Med. Imaging Graph. 61 (2017) 2–13, https://doi.org/10.1016/j.compmedimag.2017.06.001.
[37] P. Schober, C. Boer, L.A. Schwarte, Correlation coefficients: appropriate use and interpretation, Anesth. Analg. 126 (5) (2018) 1763–1768, https://doi.org/10.1213/ANE.0000000000002864.
[38] H. Akoglu, User's guide to correlation coefficients, Turk. J. Emerg. Med. 18 (3) (2018) 91–93, https://doi.org/10.1016/j.tjem.2018.08.001.
[39] M.M. Mukaka, Statistics corner: a guide to appropriate use of correlation coefficient in medical research, Malawi Med J 24 (3) (2012) 69–71.
[40] R. Dodmane, G. Aithal, S. Shetty, Construction of vector space and its application to facilitate bitwise XOR – Free operation to minimize the time complexity, J. King Saud. University - Comput. Infor. Sci. (2022), https://doi.org/10.1016/j.jksuci.2021.12.015.

[41] G. Bohm, R. Jaenicke, Correlation functions as a tool for protein modeling and structure analysis, Protein Sci. 1 (10) (1992) 1269–1278, https://doi.org/10.1002/pro.5560011005.
[42] G.R. Willmott, B.G. Smith, Modelling of resistive pulse sensing: flexible methods for submicron particles, The ANZIAM J. 55 (3) (2014) 197–213, https://doi.org/10.1017/s1446181114000066.
[43] N. Ejjigu, K. Abdelgadir, Z. Flaten, C. Hoff, C.-.Z. Li, D. Sun, Environmental noise reduction for tunable resistive pulse sensing of extracellular vesicles, Sensors and Actuators A: Phys. 346 (2022), https://doi.org/10.1016/j.sna.2022.113832.
[44] Z. Liu, J. Li, J. Yang, Y. Song, X. Pan, D. Li, Improving particle detection sensitivity of a microfluidic resistive pulse sensor by a novel electrokinetic flow focusing method, Microfluid Nanofluidics 21 (1) (2016), https://doi.org/10.1007/s10404-016-1836-9.
[45] B.S. Bull, M.A. Schneiderman, G. Brecher, Platelet counts with the coulter counter, Am. J. Clin. Pathol. 44 (6) (1965) 678–688, https://doi.org/10.1093/ajcp/44.6.678.
[46] G.T. Roberts, S.B. El Badawi, Red blood cell distribution width index in some hematologic diseases, Am. J. Clin. Pathol. 83 (2) (1985) 222–226, https://doi.org/10.1093/ajcp/83.2.222.
[47] A. Saleem, M. Husheem, P. Härkönen, K. Pihlaja, Inhibition of cancer cell growth by crude extract and the phenolics of Terminalia chebula retz. fruit, J. Ethnopharmacol. 81 (3) (2002) 327–336, https://doi.org/10.1016/s0378-8741(02)00099-5.
[48] W. Bult, S.G. Kroeze, M. Elschot, P.R. Seevinck, F.J. Beekman, H.W. de Jong, D. R. Uges, J.G. Kosterink, P.R. Luijten, W.E. Hennink, A.D. van het Schip, J.L. Bosch, J.F. Nijsen, J.J. Jans, Intratumoral administration of holmium-166 acetylacetonate microspheres: antitumor efficacy and feasibility of multimodality imaging in renal cancer, PLoS ONE 8 (1) (2013) e52178, https://doi.org/10.1371/journal.pone.0052178.
[49] M.M. Arimi, Particle size distribution as an emerging tool for the analysis of wastewater, Environ. Technol. Rev. 7 (1) (2018) 274–290, https://doi.org/10.1080/21622515.2018.1540666.
[50] A.V. Jagtiani, J. Zhe, J. Hu, J. Carletta, Detection and counting of micro-scale particles and pollen using a multi-aperture Coulter counter, Measure. Sci. Technol. 17 (7) (2006) 1706–1714, https://doi.org/10.1088/0957-0233/17/7/008.
[51] R.J. Olson, D. Vaulot, S.W. Chisholm, Effects of environmental stresses on the cell cycle of two marine phytoplankton species, Plant Physiol. 80 (4) (1986) 918–925, https://doi.org/10.1104/pp.80.4.918.
[52] H.S. Moon, S. Eda, A.M. Saxton, D.W. Ow, C.N. Stewart Jr., An efficient and rapid transgenic pollen screening and detection method using flow cytometry, Biotechnol. J. 6 (1) (2011) 118–123, https://doi.org/10.1002/biot.201000258.
[53] S. Fujiyoshi, K. Yarimizu, Y. Miyashita, J. Rilling, J.J. Acuna, S. Ueki, G. Gajardo, O. Espinoza-Gonzalez, L. Guzman, M.A. Jorquera, S. Nagai, F. Maruyama, Suitcase Lab: new, portable, and deployable equipment for rapid detection of specific harmful algae in Chilean coastal waters, Environ. Sci. Pollut. Res. Int. 28 (11) (2021) 14144–14155, https://doi.org/10.1007/s11356-020-11567-5.